metals

MDPI

Article

Assessing Microstructure-Local Mechanical Properties in Friction Stir Welded 6082-T6 Aluminum Alloy

Hossein Monajati [1,*], Mariem Zoghlami [1], Amevi Tongne [2] and Mohammad Jahazi [1]

[1] Department of Mechanical Engineering, Ecole de Technologie Supérieure, 1100 Notre-Dame Street West, Montreal, QC H3C 1K3, Canada; mariem.zoghlami1@gmail.com (M.Z.); Mohammad.Jahazi@etsmtl.ca (M.J.)

[2] École Nationale d'Ingénieurs de Tarbes, Laboratoire Génie de Production, M2SP, 47 Avenue d'Azereix, 65000 Tarbes, France; amevi.tongne@enit.fr

* Correspondence: monajati@gmail.com; Tel.: +1-514-396-8974

Received: 22 August 2020; Accepted: 11 September 2020; Published: 16 September 2020

Abstract: The severe deformation and temperature paths in the stir zone, also called weld nugget, of friction stir welded joints result, at very local levels, in significant microstructural variations, such as major differences in grain size or precipitation. One of the most common features of friction stir welds is the presence of successive material layers, known as onion rings; however, little data is available on the mechanical properties of the different regions of the weld nugget, and particularly within the onion ring bands. Such information becomes very important for the integrity of large size friction stir welded structures. In the present study, a comprehensive characterization of onion rings produced during friction stir welding of a 6082-aluminum alloy was carried out. Advanced techniques such as in-situ SEM nanoindentation, EBSD, and high-resolution EDS were used to validate and compare the characteristics of the different bands in the onion rings. The analyses consisted of quantifying variations in grain size, precipitate composition and distribution, crystallographic orientations, and mechanical properties in each band. Furthermore, the tensile strengths of different regions of the weld nugget were evaluated using shear punch testing and correlated with those for the onion ring region in order to determine the impact of the presence of onion rings on weld nugget mechanical properties. The main difference between the alternate bands in the onion ring was found to be due to the difference in their grain size, misorientation, and precipitate content. It was also observed that the bands originate from the base metal and stir zone successively due to the nature of the stirring process, which pulls BM into SZ. Comparison of the shear punch testing results in different regions of the nugget revealed that, in spite of having local differences in the hardness of alternate bands in the onion ring, the presence of onion rings has no significant impact on the deterioration of the mechanical properties of the weld nugget.

Keywords: characterization; aluminum alloys; friction stir welding; onion rings; nanoindentation; shear punch

1. Introduction

The 6000 series aluminum alloys are commonly used in transportation industries due to their high strength along with good formability and weldability. These alloys could be welded using fusion welding technologies; however, the presence of a solidified structure in a joint could present design challenges for critical applications. In this context, Friction Stir Welding (FSW), as a solid-state joining technology, has proven to be an excellent alternative to fusion-based joining technologies for such applications. Since its introduction in the early 1990s, extensive research has been conducted on various aspects of the FSW. A large amount of data is now available on the influence of process parameters on weld mechanical properties for a wide spectrum of alloys [1–5], tool and fixture design [6–10],

fundamental aspects related to material flow [11–14], modeling and simulation [15–20], etc. In recent years, with the progress made on better understanding of the interactions between process parameters and joint integrity, it has become possible to develop solid links between the above parameters, thereby ensuring the production of sound FSW joints for a wide range of industrial applications. In a very recent publication, Meng et al. [21] have provided a comprehensive review of the approaches that could be used to obtain high integrity joints with minimal thickness variations, superior mechanical properties, and in-service behavior.

Three distinct zones could be identified on the two sides of an FSW joint [22]: the heat-affected zone (HAZ) is the zone adjacent to the base metal and is only affected by the heat of welding; the thermomechanically affected zone (TMAZ) is the intermediate zone which is both affected by the heat of welding and partially deformed under the effect of the FSW tool rotation; the third zone is the weld nugget (WN), which corresponds to the zone located under the shoulder and undergoes the most severe plastic deformation and high temperatures [23] because of the stirring effect (which is the most distinctive feature of the FSW process) brought by the rotation of the tool and the shoulder [21]. The properties (mechanical, corrosion, etc.) of a FSW joint are therefore very much dependent on the characteristics of each of the above three zones and their mutual interactions. For example, it is well-known that in FSWed precipitation-hardened aluminum alloys, the TMAZ is the 'weak link', and significant efforts been devoted to better understand the mechanisms of precipitation and develop solutions [24,25]. In the case of weld nugget, the presence of high strains, strain rates, and temperatures result in the occurrence of significant microstructural changes such as dynamic recrystallization [26–29], second phase dissolution and reprecipitation [24,30–32], and phase transformations, e.g., in Ti or ferrous alloys [22,33]. However, due to the very complex thermomechanical pattern present in different zones of the weld nugget, often a non-homogeneous microstructure is observed in this zone. For instance, while dynamic recrystallization produces significant grain refinement, atypical grain growth could also occur in some regions, resulting in the formation of microstructures that would be unreliable under fatigue loading [34].

Another microstructural feature associated with the weld nugget that has been reported since the introduction of the FSW technology is the presence of banded structures, more commonly known as onion rings (OR) [35]. These bands are observable under an optical microscope and have concentric circular shapes in the *transverse plane* of the weld. While some researchers have considered ORs as possible defects with possible deleterious effects on the mechanical properties of the FSW joint [36], others have seen them more as a consequence of material flow without impact on joint properties [37]. Krishnan [38] reported that the formation of ORs is due to the simultaneous action of the tool advancement and rotation. Colligan [39], using a stop-action technique, observed that the material in the weld is not totally stirred and only a fraction of it is extruded. He related the formation of the banded structure to the extruded material and justified his analysis in terms of the movement of the stirred metal from the top of the weld towards the tool, which would force the material located in the lower part of the advancing side of the nugget to extrude to the retreating side and then upward with the advancement of the tool. Mahoney et al. [40] related the formation of ORs in a FSWed 7075-T651 aluminum alloy to the difference in grain size and changes in local density distribution of the precipitates' density. Hamilton et al. [41] reported that differences in precipitate density were at the origin of the formation of ORs. A difference in precipitation density of the banded structure was also observed by Sutton et al. [42,43]; however, the observations were made on the parallel plane of the weld, i.e., the semi-cylindrical traces left by the tool along the surface of the piece and not on the weld transverse plane. Fonda et al. [44] observed a difference in grain orientation and pure shear texture between the OR bands in FSWed Aluminum alloy AA2195. The texture variation was related to the periodic extrusion performed by the tool and its possible effect on the generation of the ORs through the thickness of the weld. Similar findings were reported by Prangnell and Heason [45] in a study of the same alloy. They attributed the formation of the ORs to a perturbation of the material flow whenever the face of the tool carried the material in the retreating side. However, the authors did not

make correlations between grain size variation or precipitates' evolution within the bands and the mechanical properties of the bands or the weld nugget. Schneider and Nunes [46] also observed the alternation of grain orientation between the different bands and attributed the formation of ORs to an oscillation between complex maelstrom and straight-through flow. Here again, the characteristics of the ORs layers and their impact on different regions of the weld nugget were not studied.

The above review illustrates well that despite the diverging opinions on the possible impact of the ORs on mechanical properties, few studies are available on the microstructure-mechanical properties characteristic of each layer in the OR and its impact on *local* tensile properties of FSW joints (i.e., nugget zones with or without OR), and in particular, it is not clear how the presence of ORs in the weld nugget would affect its mechanical properties. Most of the available data is on *global* determination of the mechanical properties through conventional or sub-size tensile testing [47–50].

In the present work, in a first step, the mechanical and microstructural characteristics of different layers in the ORs at the scale of few grains were determined and their interrelationships studied. Then, the mechanical properties of the different regions of the weld nugget, at the scale of 1–2 mm, were examined, and the influence of the presence of ORs on the local mechanical properties was determined. Finally, the obtained results were compared with the macroscopic tensile properties of the base metal.

2. Experimental Procedure

The material used in the study included 6 mm thick 6082-T6 aluminum alloy plates (250 × 120 mm) with the nominal composition provided in Table 1. Figure 1 shows the experimental setup used in the present study. Two types of pin and tool geometries were used to produce different size and extent of ORs. It must be noted that, based on the objective of the study, the processing parameters were selected so as to produce the largest possible ORs rather than determining the optimum processing conditions to produce defect-free joints with the highest mechanical properties. The larger size ORs produced in the joints facilitated their reliable characterization. The first series of FSWed samples were produced using a trigonal pin with 6 mm diameter on the top and 4 mm diameter at the bottom. The tool was made with commercially grade tungsten carbide and had a shoulder diameter of 12 mm and a total height of 5.5 mm. The second series of samples were produced using a simple conical tool with a shoulder diameter of 15.8 mm and a 5 mm diameter on the top and 1.77 mm diameter at the bottom. Table 2 shows the welding parameters.

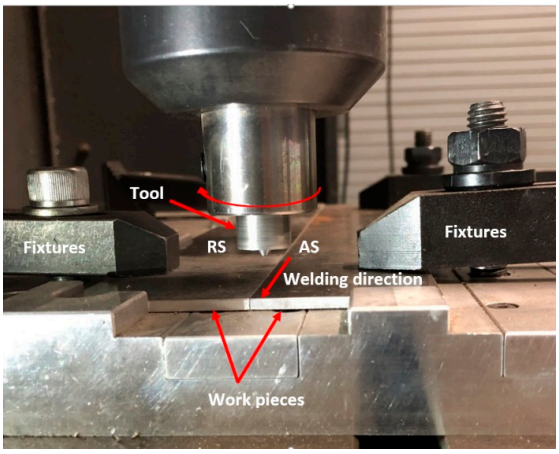

Figure 1. The experimental setup used in the present study (Bridgeport Interact 400, Connecticut, CT, USA).

Table 1. Nominal composition of the alloy used in the investigation (wt%).

Alloy	Al	Si	Fe	Cu	Mn	Mg	Cr	Zn	Ti
Al 6082	Balance	0.7	0.5	0.1	0.4	0.6	0.25	0.2	0.1

Table 2. Welding parameters used in the present study.

Sample Code	Tool	Rotational Speed (RS) (rpm)	Travel Speed (TS) (mm/min)	RS/TS Ratio
T1	trigonal	1500	400	3.75
T2		1500	300	5
T3		2000	600	3.33
T4		1750	200	8.75
C1	conical	1750	200	8.75

Metallographic samples were prepared from different cross-sections along the joint. Microstructure examinations were carried out on polished samples using conventional metallographic techniques. Revealing the microstructure of the different zones of the nugget, particularly the OR zone is quite challenging. This is due to the fact that the microstructure of the weld nugget is characterized by a very complex deformation pattern changing drastically at a local scale from one zone to another. This is even more acute when it comes to the OR region where significant changes are present over a few micrometers in strain distribution, grain size, crystallographic orientation, and precipitate distribution. All these microstructural features render the etching process very challenging. In the present work, a methodology was developed and optimized to clearly reveal the boundaries between the ORs and highlight the grain boundaries in each band. The method consisted in a two-step etching approach starting with etching for 30 s in Barker solution (5 mL HBF_4 + 200 mL H_2O) followed by drying of the sample and then immersion in the Weck solution (100 mL H_2O + 4 g $KMnO_4$ + 1 g NaOH) for 5 to 7 s. Preliminary optical metallography analysis indicated the presence of large size alternating bands in the joints produced by the trigonal pin while very narrow and discontinuous ORs were observed in the samples welded by the conical tools. Thus, the study was focused on the samples produced by the trigonal tool.

Detailed microstructural studies carried out using the Hitachi SU8230 Cold Field Emission Gun Scanning Electron Microscope (CFEG-SEM) (Hitachi, Minato, Tokyo, Japan) Observations of grain morphologies and precipitates distributions were made on both secondary and back-scattered modes and the Electron Back Scattered Diffraction analysis was done using a Bruker Quantax® model camera (Bruker Corporation, Billerica, MA, USA). For the EBSD study, after standard metallographic preparation, the samples were polished for 24 h in a Vibromet® (Buehler, Lake Bluff, IL, USA) polishing machine with 0.05 µm colloidal silica in order to obtain a very high-quality stress-free surface condition. Nano-indentation tests were performed using a Hysitron's PI series indenter (Bruker Corporation, Billerica, MA, USA) installed in the SU-8230 SEM to measure the local hardness in the banded structure. The chemical compositions of the precipitates were revealed by Energy Dispersive Spectroscopy (EDS) using a Quad® detector (Bruker Corporation, Billerica, MA, USA) on the SU-8230 SEM. Shear punch tests were carried out according to ASTM STP 888. The details regarding the testing procedure are provided in Reference [51]. The dies and punch were designed and manufactured using precision machining. The punch had a flat cylindrical head and a diameter of 1 mm with a maximum 10 µm allowable space between the die and the punch. Figure 2 shows the shear punch testing set-up used in the present study.

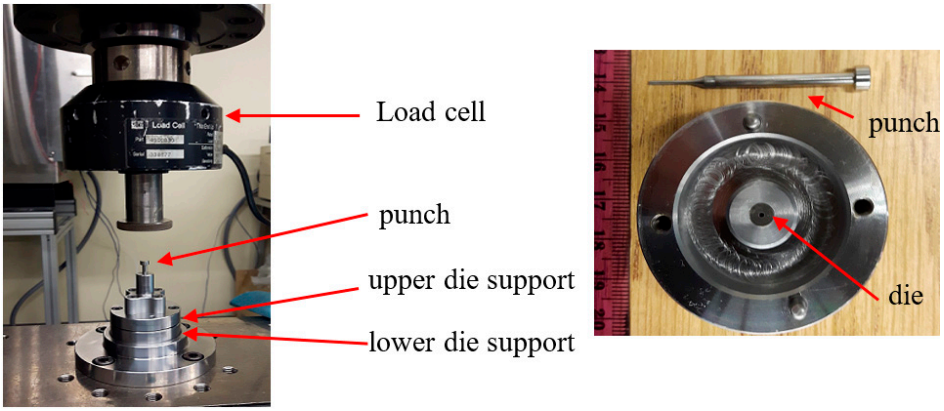

Figure 2. Shear punch test set-up.

The shear stress τ was calculated using the following Equation [50]:

$$\tau = \frac{P}{2\pi r_{avg} t} \quad (1)$$

where P is the applied load, r_{avg} is the average radius of the die and the punch and t is the specimen thickness. A compression testing machine (MTS model Alliance RF/200 with the 10 KN load cell, MTS corporation, Eden Prairie, MN, USA) was used for the shear punch tests. The normalized displacement was calculated by dividing the displacement by the specimen thickness. Yield shear stress τ_{ys} and ultimate shear stress τ_{us} were obtained from the shear stress versus normalized displacement curve. Yield tensile stress (YTS) σ_{ys} and ultimate tensile stress (UTS) σ_{us} were respectively calculated using the following equations [50]:

$$\sigma_{ys} = 1.77\tau_{ys} \text{ and } \sigma_{us} = 1.8\tau_{us} \quad (2)$$

For each condition, at least five shear punch tests were conducted, and the average value was used for the determination of the tensile strength. Finally, it must be noted that initially, uniaxial tensile tests, according to ASTM E8 standard, were carried out on the as-received material, and the results were compared with those obtained using shear punch tests. A very good agreement, less than 1% difference in Yield stress and UTS, were obtained between the two methods, thereby confirming the calibration of the method and the validity of the above coefficients for application to the investigated alloy. Details of the calibration method and repeatability teste are provided in Reference [52].

3. Results and Discussion

3.1. Microstructure

In an initial step, the microstructure of all tested samples was examined, and it was found that the widest and most visible ORs were present in sample T4. As a result, in order to facilitate the analysis and interpretation of the results, only sample T4 was considered for comprehensive examination and the other samples were used for comparison purposes. Figure 3a,b shows optical micrographs of sample T4 where the ORs were present in the advancing side as alternated dark and light bands. A schematic representation of the weld cross-section showing different areas of microstructure examinations is presented in Figure 3c. Finally, a magnified view of the OR region is presented in Figure 4, where each band could be clearly distinguished.

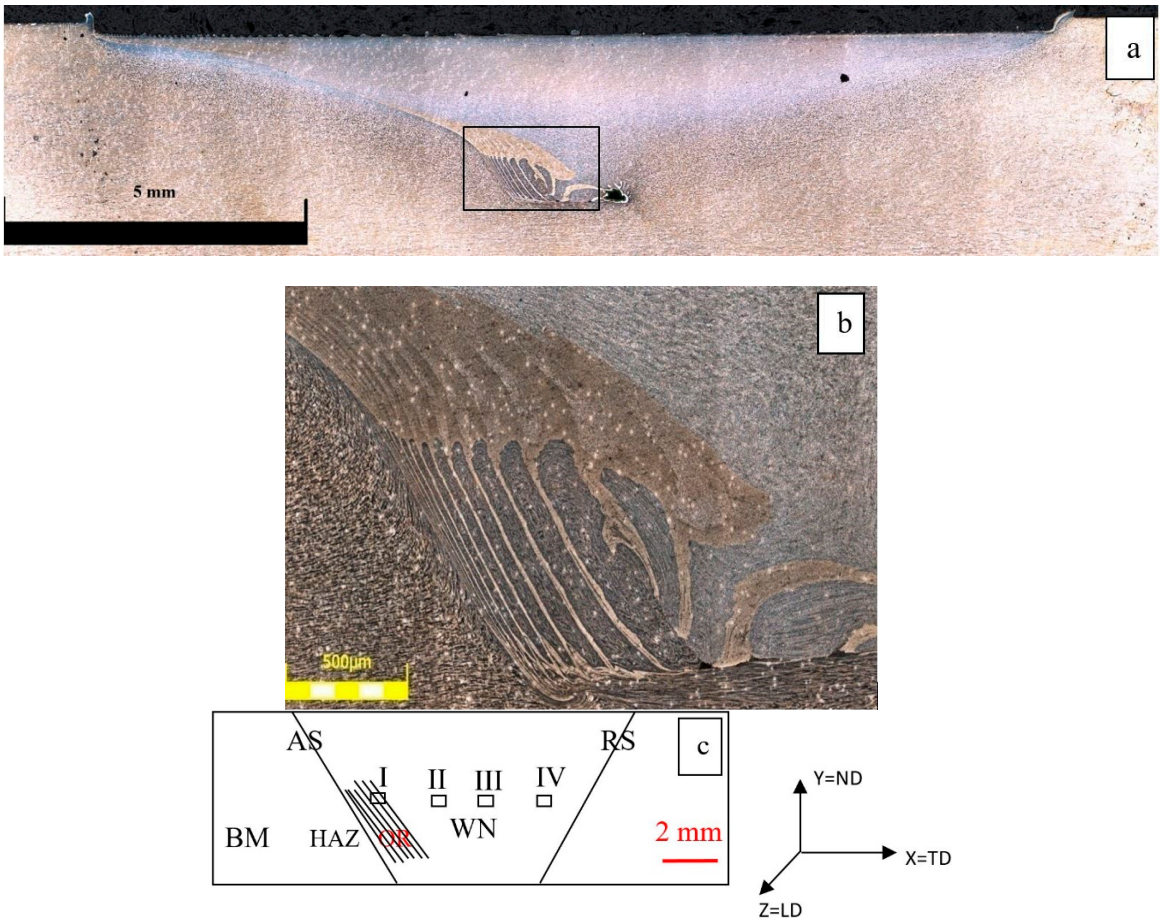

Figure 3. (**a**) Cross-sectional macrostructure of Sample T4; (**b**) optical micrograph of the OR zone; (**c**) schematic representation showing different locations of microstructure examinations. BM: base metal, AS: advancing side, RS: retreating side, WN: weld nugget, HAZ: heat affected zone, ND: normal direction, TD: transverse direction, LD: longitudinal direction.

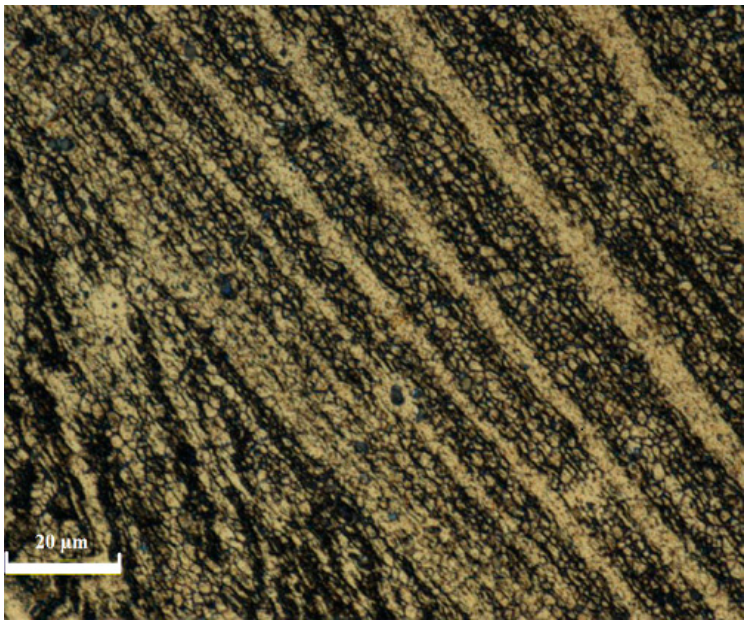

Figure 4. Magnified view of the zone containing ORs in sample T4.

The WN was characterized by very fine equiaxed grains; however, their sizes varied according to their position in the weld. It was specifically noticed that grain sizes in the dark and light bands are different. Figure 5a,c,e shows illustrative examples of grain sizes in the dark and light bands of the ORs. The average grain size was about 3 µm in the dark band, while it was about 7 µm in the light bands. To better quantify the grain size variation in the bands, the proportions of grains with diameter less than 3 µm, between 3 µm and 6 µm, and above 6 µm were calculated. It was found that bands with small grains (i.e., dark bands) contained about 64% grains under 3 µm, while this proportion was only 29% in the light bands (i.e., larger grains). Furthermore, and for comparison purposes, Figure 5b,d,f shows the grains in the retreating side of the same samples, with no presence of ORs. The average grain size in the retreating side was about 8.5 µm, which is significantly larger than the average grain size (about 3 µm) observed in the dark bands of the ORs. Therefore, it can be concluded that there is a clear difference in grain size distribution between the dark and light bands of the OR, and that the average grain size in the OR is smaller than the grain size in the retreating side of the weld.

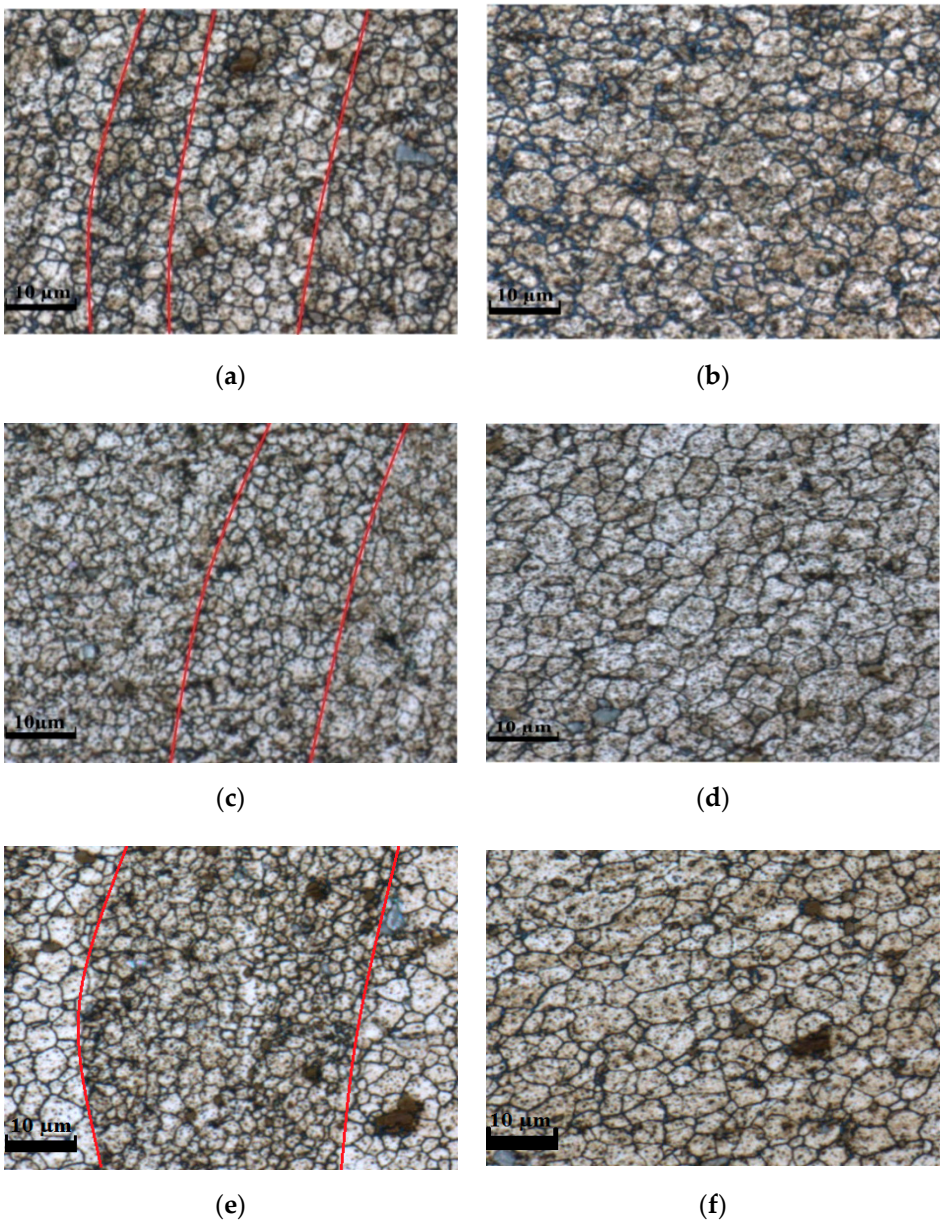

Figure 5. (**a**,**c**,**e**) are onion rings; (**b**,**d**,**f**) are areas in the retreating side in samples T1, T3, and T4, respectively.

3.2. EBSD Analysis

The inverse pole figure (IPF) maps and the misorientation distribution maps of the examined areas (I to IV) shown in Figure 3c are illustrated in Figure 6. As it can be seen, base metal (BM) consists of pancaked grains with their main axis = 0°, with the majority of the grains free from low angle boundaries (2–10° misorientation), characteristic of annealed Al alloys (Figure 6a,b). Coming into the WN, the material rotates around the tool, becomes highly deformed at high temperatures, and starts to recrystallize, while the trace of parent grains could still be recognized from the colors, as observed in the microstructures of areas II and III (WN interior), in Figure 6e,g. In fact, all the recrystallized grains, nucleated from the same parent grain, show similar orientation (color) and form a banded structure with a 45° axis, representing material flow inside the WN (shown by dashed arrows). The misorientation maps of these two areas (Figure 6f,h) also show that parent grains have become fragmented and the recrystallized grains have been formed from subgrain rotations indicative of the continuous recrystallization occurrence.

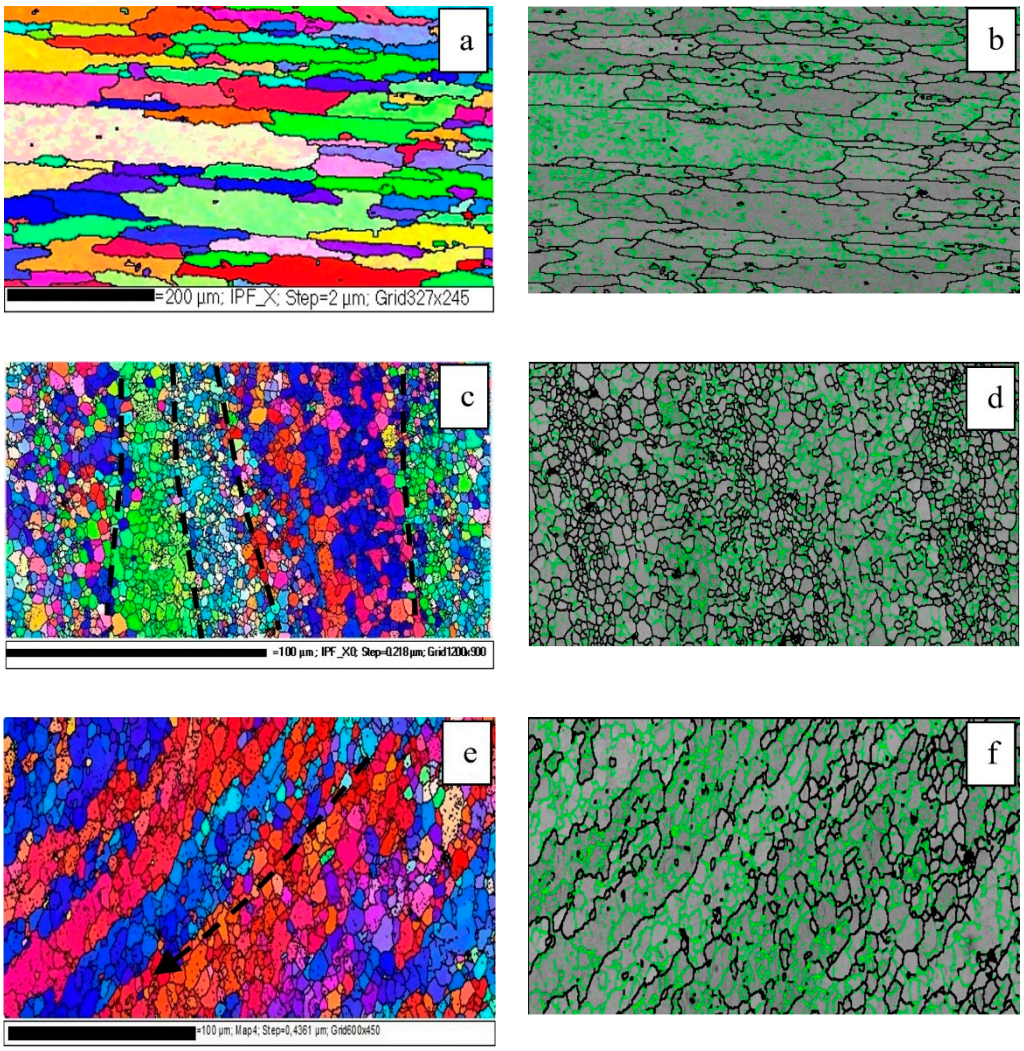

Figure 6. *Cont.*

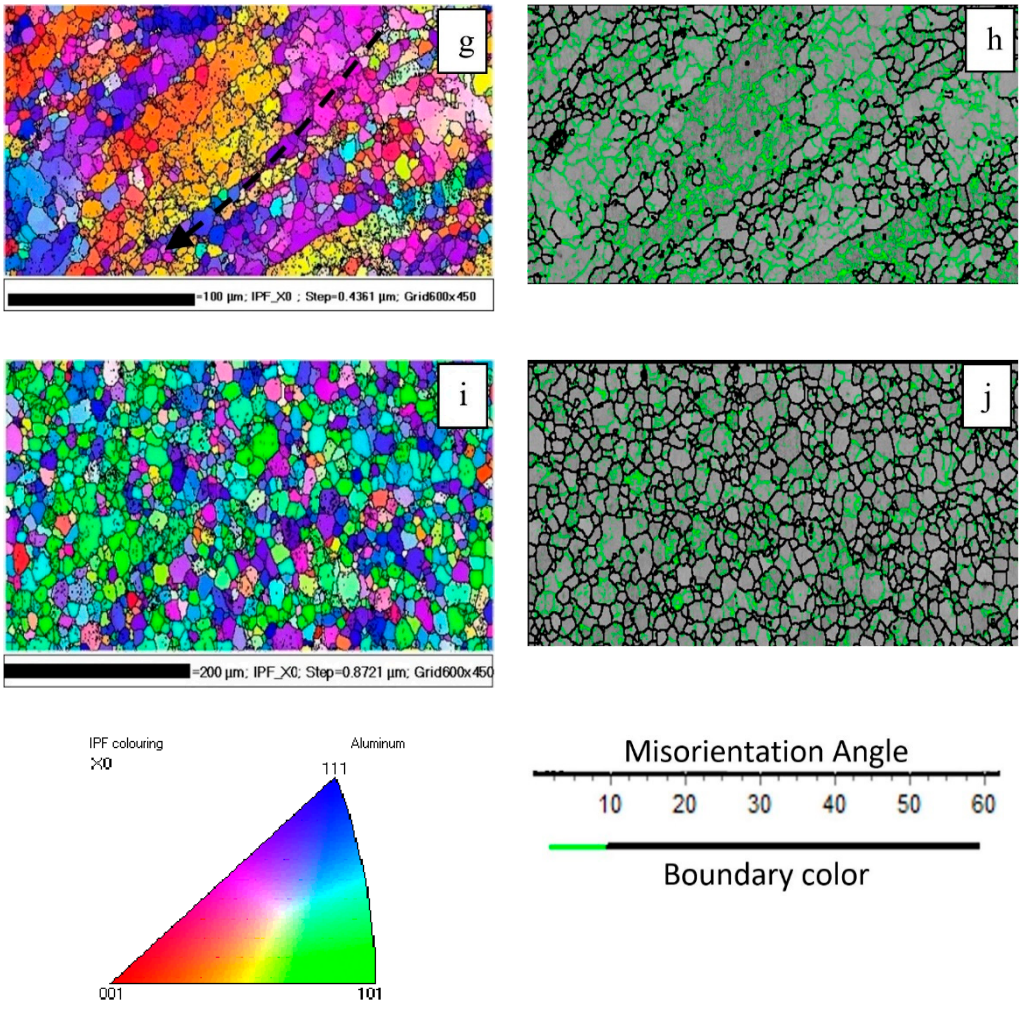

Figure 6. IPF-X maps of different areas of the weld. BM: (**a**,**b**); onion rings (area I): (**c**,**d**); weld center (area II): (**e**,**f**); weld center (area III): (**g**,**h**); RS (area IV): (**i**,**j**).

The results also show that almost all the coarse grains contain low angle boundaries, proving that continuous rotation of subgrains was ongoing, while finer grains can be seen without or with slight low angle misorientation indicating completion of recrystallization in those regions. Close to the WN-BM border (area I), the banded structure becomes more pronounced (manifested as OR) with more progress of recrystallization and formation of finer grains (Figure 6c). Here again, recrystallized grains are free from low-angle boundaries, while the coarse ones still contain them (Figure 6d). The axis of the banded structure also rotates from 45° (in area II) to almost 90° (up-down). This finding could be attributed to the severe friction between the visco-plastic material flowing inside WN and the solid material of BM. Recrystallization progressed by progressive material flow from AS toward RS and spread over almost the entire microstructure of the WN. Limited grain growth was also observed in some regions, as shown in Figure 6i,j.

The IPF contour maps of Figure 6 displaying texture evolution in the areas I to IV are illustrated in Figure 7. As it can be seen in Figure 7a, BM shows a preferred orientation of 001 poles around *Z*-axis (which is aligned with the transverse direction of the rolled sheet, Figure 3c), with a maximum intensity of 3.7. This texture becomes more intensified in the WN (area II, Figure 7c) and then rotates, resulting in the intensification of the 111 poles around *Y*-axis with a maximum intensity of 3.5 in area I in the OR zone (Figure 7b). The texture remains steady from AS to RS, as it is observed in IPF contour of area IV, which is very similar to area I with a slightly higher intensity of 4.3 (Figure 7e).

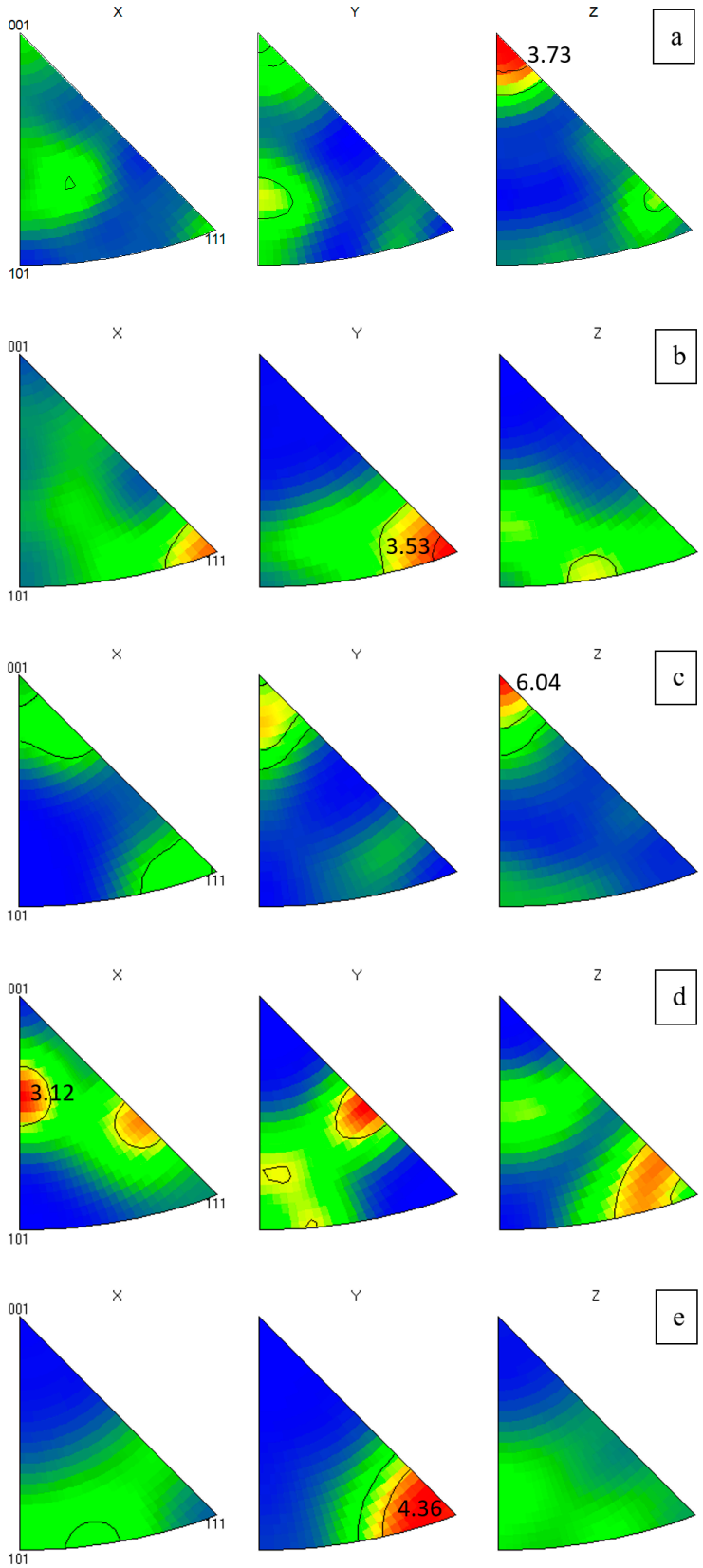

Figure 7. IPF contour maps of Figure 6 representing (**a**) BM, (**b**) Area I, (**c**) Area II, (**d**) Area III, and (**e**) Area IV.

A comparison between the light and dark bands observed in optical metallography examinations (Figure 5a) and the colored bands of IPF maps (Figure 6c) suggests a possible correlation between these two observations. However, detailed examination of many samples revealed that the boundaries identified in optical metallography did not necessarily match with the ones in the EBSD maps. In fact, the dark contrasts in optical metallography appeared to be originating from the etching of fine recrystallized grains with high density of high-angle grain boundaries (HAGB) which scatter the light more than the areas containing coarser grains and lower density of HAGB (lighter color).

In contrast, the color difference between the regions in the EBSD maps appears to originate from the parent grains' orientations, which keep their orientations even after recrystallization. Therefore, a direct correlation could not be made between the observed dark and light bands in the optical metallography with the banded color contrasts observed in the EBSD analysis. This is an important finding because the similarities between the dark and bright bands under an optical microscope and EBSD mapping could be misleading. Hence, other features, as described in the following, must be studied in order to determine the commonalities and differences between the bands.

3.3. In-Situ Nanoindentation in the Banded Structure

To determine the hardness profile in OR, Area I was studied by nanoindentation crossing the banded structure, as shown by the equidistant black spots in IPF map of Figure 8a. Two rows of indentation were carried out for repeatability purpose and the obtained profiles are presented in Figure 8b. It should be mentioned that as EBSD was performed after nanoindentation, the indents were not indexed in EBSD due to heavy local deformation and denting. As it can be observed in the hardness profile, the majority of the measured values are around 90 HV on both lines with few points showing a noticeable drop in hardness up to 30 HV. However, no correlation could be made between the lower hardness values and the position of alternate EBSD colored bands, showing that the hardness values were not affected by changes in grain orientation.

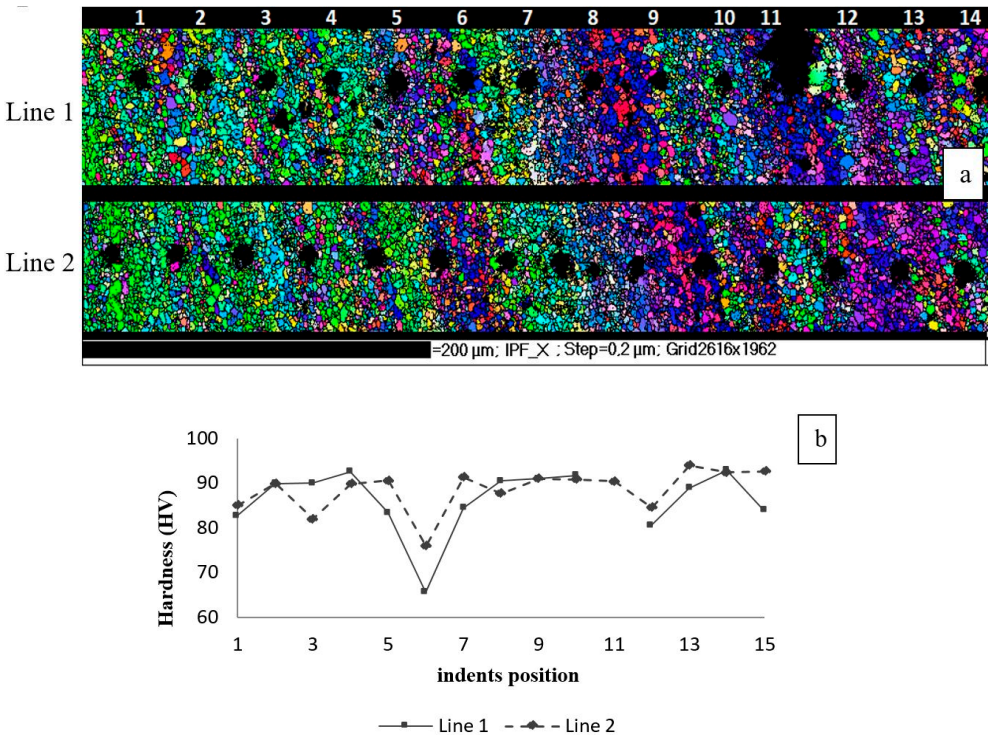

Figure 8. (**a**) IPF map of the banded structure and (**b**) hardness profile in the banded structure area.

A detailed examination of the grain structure around the indents revealed that most of the high hardness values were obtained in the fine grain zones and the lower hardness values in the coarser grain ones. An illustrative example is shown in Figure 9, where a higher magnification and resolution for indents number 5 and 6 on line 1 is shown and the finer structure of grains around indent 5 is visible. The evolution of the hardness appears then more related to a Hall-Petch effect rather than crystallographic orientation of the grains. However, it is difficult to accurately quantify the contribution from the grain size changes to the hardness of each indent in Figure 8. For example, according to Hall-Petch relationship between grain size and strength, a 50% bigger grain size around indent number 6 in comparison to indent 5 is expected in order to have a 15 HV drop in hardness; however, experimental measurements show ~30 HV drop, indicating that other factors contributed to the hardness drop. It should be mentioned that a similar behavior was also observed for line 2, but is not detailed here as the conclusions are identical.

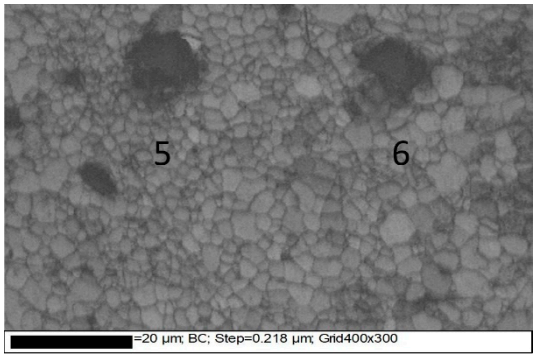

Figure 9. EBSD band contrast map of the area around indents 5 and 6 on line 1. The non-indexed dark spots correspond to the indent locations.

3.4. EDS Analysis

Another contributing factor to the changes in the hardness could be precipitation hardening. This could be particularly the case for the 6XXX series aluminum alloys, where precipitates play a significant role in the evolution of the hardness [53]. In order to validate this possibility, the high-resolution low-voltage EDS technique (at 5 kV), using a Quad detector with a very short distance of 2 mm to the sample, installed in FE-SEM, was used to study elemental distributions around the indents, providing an assessment of the distribution of chemical elements in the microstructure. It must be mentioned that in addition to EDS, Differential Scanning Calorimetry (DSC) combined with the X-Ray diffraction technique has also been used to study precipitate evolution in the different zones of FSW joints of precipitation-hardened alloys, as reported in a recent publication by Jandaghi et al. [24].

The obtained EDS maps around indents 5 and 6 are presented in Figure 10, in which the distributions of Si, Mn, Fe and Mg, as the main constitutive elements of the precipitates are indicated. Figure 10a,c shows Mg and Si distribution around indents 5 and 6, respectively. From these figures, a distinct distribution of Mg and Si is revealed in both cases, with a higher density and relatively smaller size around indent 5. By superimposing Fe and Mn distribution maps on top of the Si (Figure 10b,d), it can be seen that Mn-rich zones match with the Si ones. In agreement with the analysis reported by Svennson et al. [54] and Liu [55], it could be assumed that the Si-rich areas in Figure 10a,c are most likely $Al_{12}(Fe,Mn)_3Si$ type precipitates, and the Mg-rich ones are Mg_2Si. The finer size and higher density of precipitates further confirms and justifies the higher hardness values measured at point 5 compared to point 6, as reported in Figure 8.

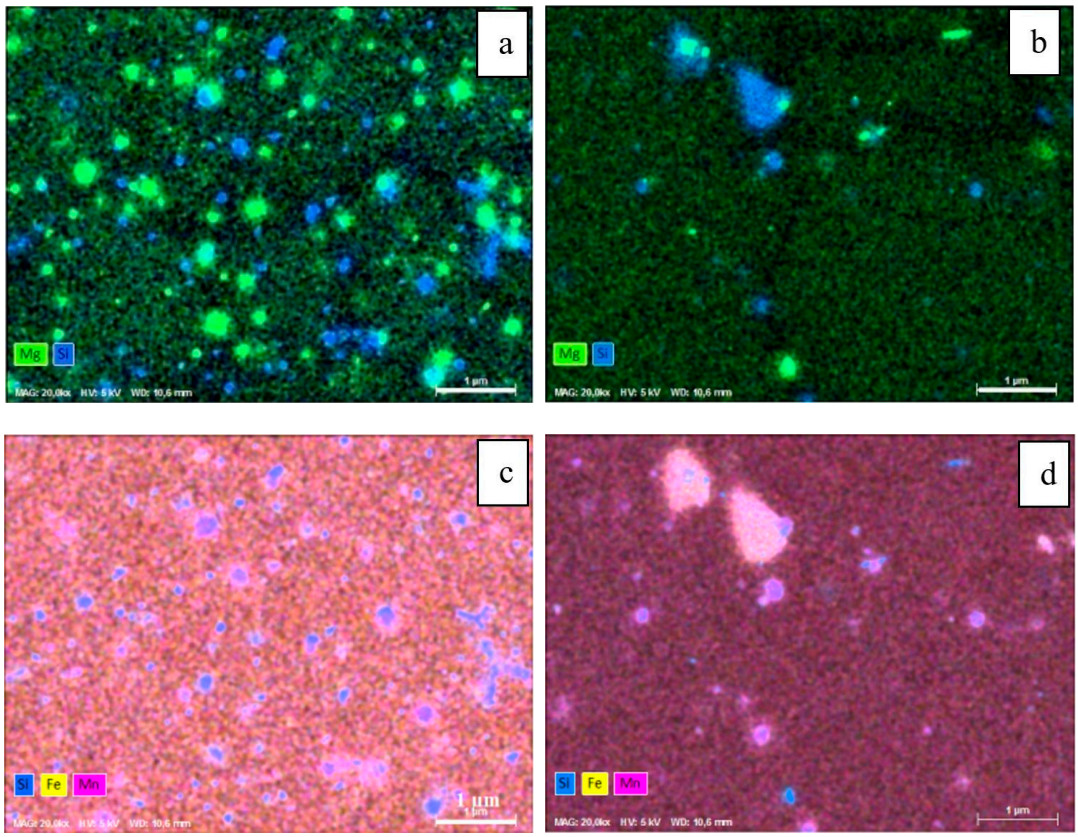

Figure 10. The distribution of Si, Mg, Fe, and Mn around (**a**,**c**) indent 5 with finer and (**b**,**d**) indent 6 with relatively coarser structure.

To further analyze the alternate precipitation nature in the OR bands, it is worth examining the EDS maps of the other areas, as indicated in Figure 11. Starting from BM, Si-Mn precipitates with sizes around 200 nm are very clear in Figure 11, while Si-Mg precipitates are smaller in size and less revealed. In the WN center (areas II and III), a much smaller number of precipitates are present, indicating that precipitate dissolution had taken place. In the retreating side, again both Si-Mg and Si-Mn precipitates could be observed although the Si-Mg ones are clearer, probably indicating a re-precipitation process.

The above observations can be explained in terms of the impact of the thermal history experienced in different locations of the joint on precipitate dissolution, re-precipitation, and coarsening. Specifically, De Fillipis et al. [56] studied the evolution of surface temperature during FSW of a 5754-H111 aluminum alloy using the thermography technique and correlated the temperature profiles to mechanical properties. Tang et al. [57] studied the temperature evolution through the thickness of a 6 mm thick 6xxx series aluminum alloy by inserting K-type thermocouples at different depths below the pin and showed that there was a clear temperature gradient through the thickness of the plate. Similar results have also been reported by Liu and Ma [58], who studied the thermal cycles experienced by the low hardness regions in FSWed 6 mm thick 6061 aluminum alloy plates. They found that there was a temperature gradient through the thickness and that the thermal regime was at the origin of the changes in the density of the precipitates, thereby affecting the hardness evolution of the joint. Other studies by Woo et al. [59], Sato et al. [60], and Frigaard et al. [61] either experimentally or by modeling have also confirmed the presence of a thermal gradient through the thickness and its influence on the dissolution, re-precipitation, and coarsening of the precipitates in 6061 aluminum alloys or other precipitation hardening aluminum alloys. In the present work, the dissolution of precipitates in the WN center could be related to adiabatic heating generated by deformation which could bring the temperature in the stir zone (SZ) even up to 600 °C [58,62]. However, re-precipitation could occur due to temperature decrease when coming out of the SZ in the RS, where the coarsening of recrystallized

grains also takes place. As indicated in Figure 11, the composition of particles after re-precipitation is somehow different from BM as Si-Mg precipitates are dominant when comparing RS with BM. The alternate nature of precipitation in ORs could then be explained by comparing precipitates' main constituents and quantities in Figure 10; Figure 11: it appears that the precipitates are similar to RS in one band (Figure 10a,c around indent 5) and to BM in the other (Figure 10b,d around indent 6). This could be related to the perturbation nature of the stirring process which pulls BM into SZ and mixes it with the already stirred material coming from RS. The phenomenon is more evident from Figure 3b, a magnified view of the ORs in Figure 3a, in which banded ORs with two distinct etching contrasts, one similar to BM and the other similar to SZ, are shown.

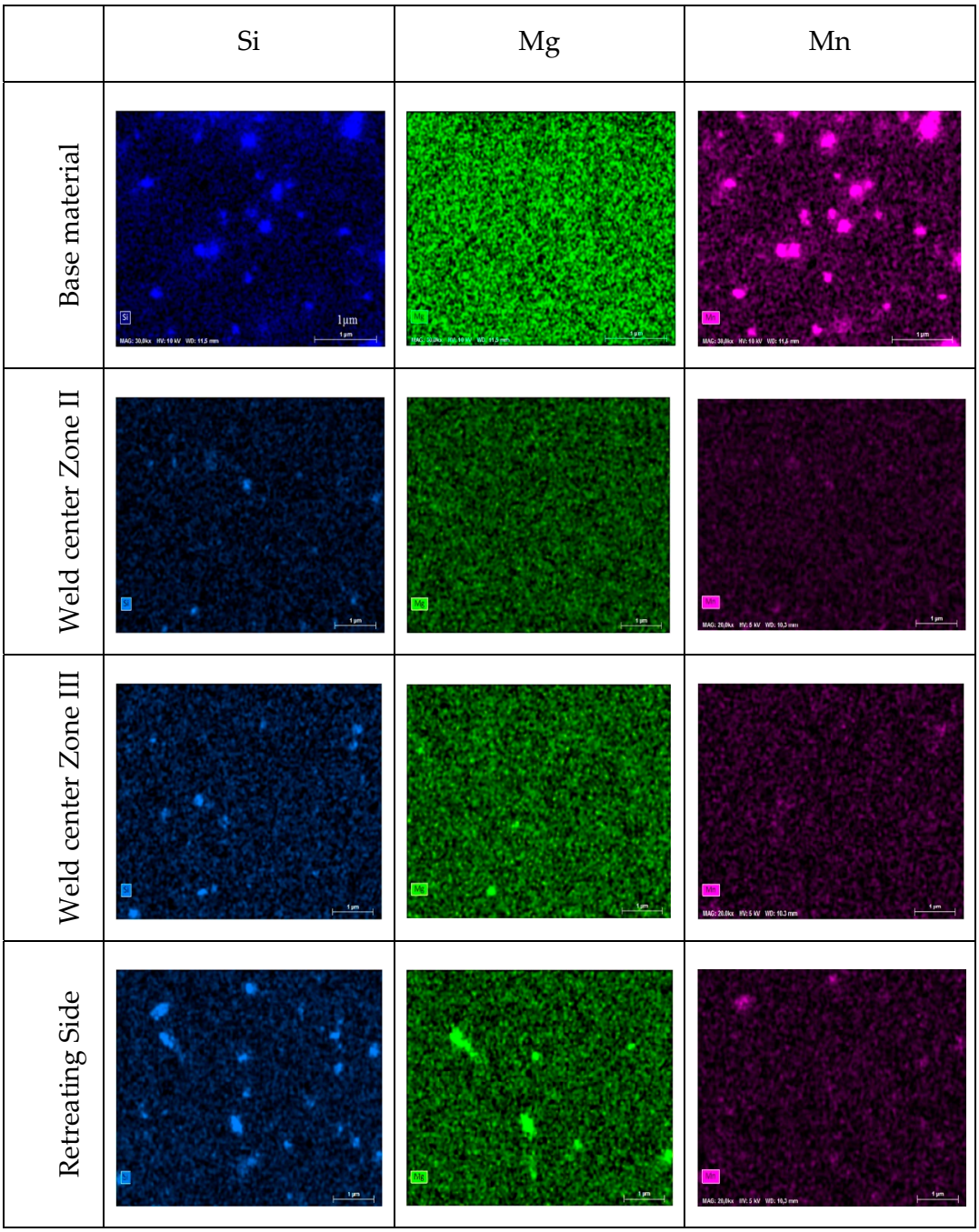

Figure 11. EDS map of Si, Mn, and Mg distribution in different areas of the WN.

Finally, it is also interesting to note that the above findings support the view of Fonda et al. [44] and Prangnell & Heason [45] that ORs are produced by periodic extrusion of new material from BM and its mixing with existing stirred material while the deformation and dynamic recrystallization of BM grains take place at the same time.

3.5. Influence of Banded Structure on Local Tensile Properties

One of the main challenges in studying the impact of the presence of ORs on mechanical properties is their small sizes and localized zones. Therefore, macroscopic evaluation of mechanical properties, which provide a global image of the joint, could not be used to quantify the impact of the presence of ORs. In the present work, shear punch tests were performed on the base metal and on different areas in the cross-section of the weld (on the top and the bottom of the weld and the HAZ in both advancing and retreating sides) of sample T4. These different areas are shown on the diagram of Figure 12 and the red circles represent the punching location. In preliminary experiments, shear punch tests were carried out on the base material and the obtained ultimate tensile strength value (365 ± 30 MPa) was compared with the one obtained from conventional tensile tests (332 ± 30 MPa), thereby confirming the validity and applicability of the shear punch technique for evaluating mechanical properties.

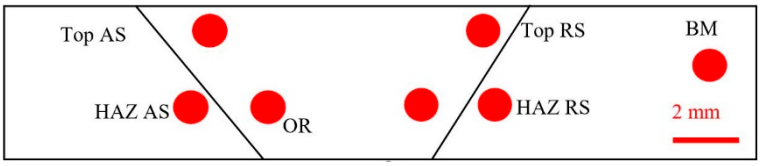

Figure 12. Shear punch test locations in sample T4.

Evaluation of Local Mechanical Properties

Table 3 shows the shear test results of different locations in the WN as well as HAZ for sample T4 obtained using shear punch tests. The results show that the mechanical properties in the top AS are higher than the remaining points in the WN as well as HAZ. Similar observations were reported by Hornbuckle et al. [63] on shear punch testing of FSWed 2139-T8 aluminum alloy. The authors found that the shear strength in the upper part of the weld had values exceeding 300 MPa, about 295 MPa at the center and 270 MPa at the bottom. However, it was observed in the present investigation and also reported by Hornbuckle et al. that the grain size at the top of the weld is larger than in the bottom and therefore the observed trend does not follow the Hall-Petch relation. The unexpected behavior was related by the authors to the thermal regime during FSW with higher temperatures on the top and gradual decrease through the thickness. The analysis presented above (Section 3.4) on the evolution of the precipitates agrees with that of Hornbuckle et al. and confirms the critical role played by temperature distribution on the evolution of mechanical properties in FSWed precipitation-hardened aluminum alloys.

Table 3. Shear stress and UTS in different locations in sample T4.

Test Location	Shear Stress (MPa)	Calculated UTS (MPa)
Top AS	179	323
Top RS	134	241
HAZ AS	124	224
HAZ RS	135	242
OR	125	225
Bottom RS	156	281
BM	220	396

The shear punch results and the data reported in Figure 13 and Table 3 also show that with the exception made for the top RS region, no major differences are observed between the mechanical properties in the OR and other regions of the WN or HAZ. This finding indicates that, despite the fact that the thermal regime and strain paths are different in the top and bottom of the WN in an FSW joint [11] and the grain sizes are different, only minor differences were observed in the mechanical properties. It is also important to note that, while it is possible with shear punch testing to obtain local mechanical properties, the deformed zone contains both dark and light zones and therefore one obtains the global mechanical properties of the OR rather than that of each band. Therefore, it can reasonably be said that the mechanical properties of the ORs as a whole are similar to other regions of the WN, and hence, ORs, despite their unique features, do not seem to be a FSW defect that can have a deleterious effect on mechanical properties.

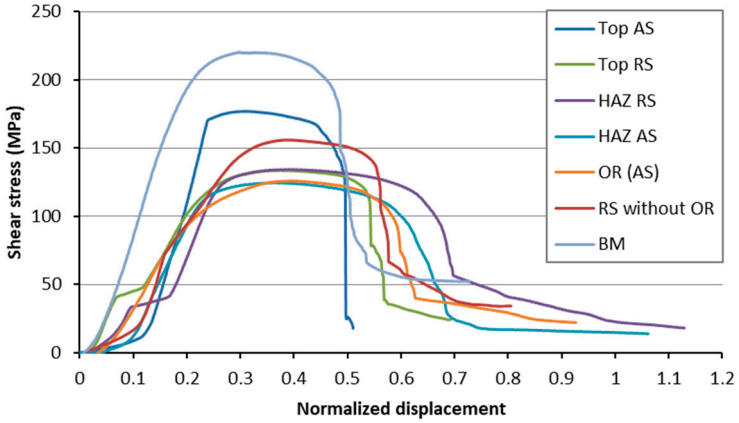

Figure 13. Shear punch test result for sample T4.

4. Summary and Conclusions

In the present study, the local mechanical properties of different regions of the weld nugget of a 6082 FSWed joint containing ORs was investigated. To better understand the impact of the presence of ORs, a comprehensive characterization of the different regions of the ORs were carried out. The following conclusions car be drawn from the present research:

(1) Both optical microscopy and EBSD analysis revealed ORs as alternating bands spreading over large distances in the weld nugget. However, no correlation exists between the patterns observed by optical microscopy and those obtained by EBSD. It was shown that despite their similarity, the observed bandings had different origins.

(2) Areas containing grains with high angle boundaries (retreating side and dark bands) were more particle-rich than those formed from grains with low angle boundaries (center of the weld nugget and light bands).

(3) In-situ SEM nano-indentation did not reveal a clear difference in hardness of the bands with different orientations, whereas a distinct difference in hardness of bands with different grain size and precipitate content was observed.

(4) Shear punch testing was used to compare the local mechanical properties of the weld nugget in the regions with or without ORs and it was determined that the presence of ORs does not seem to modify the mechanical properties of the weld nugget.

Author Contributions: M.J. conceived the project and designed the methodology; M.Z., A.T. conducted the FSW experiments; H.M. prepared the surface of EBSD samples and performed the EBSD mapping and nanoindentation; M.J., M.Z., A.T., H.M. participated in the analysis and interpretation of the results; H.M. wrote the first version of the paper that was shared with all authors for comments. M.J. supervised the project. All authors have read and agreed to the published version of the manuscript.

Funding: This research is financially supported by the National Research Council Canada (NSERC) in the framework of M.J. Discovery Grant.

Acknowledgments: The financial support of the National Science and Engineering Research Council Canada (NSERC) in the framework of the Discovery Grant is acknowledged. The support from Radu Romanica for metallographic sample preparations and Serge Plamondon for shear punch testing is very much appreciated.

Conflicts of Interest: The authors declare no conflict of interest.

References

1. Lim, S.; Kim, S.; Lee, C.-G.; Kim, S. Tensile behavior of friction-stri-welded Al 6061-T651. *Metall. Mater. Trans. A* **2004**, *35*, 2829–2835. [CrossRef]
2. Dubourg, L.; Merati, A.; Jahazi, M. Process Optimisation and Mechanical Properties of Friction Stir Lap Welds of 7075-T6 Stringers on 2024-T3 Skin. *Mater. Des.* **2010**, *31*, 3324–3330. [CrossRef]
3. Song, K.H.; Nakata, K. Effect of precipitation on post-heat-treated Inconel 625 alloy after friction stir welding. *Mater. Des.* **2010**, *31*, 2942–2947. [CrossRef]
4. Gangwar, K.; Ramulu, M. Friction stir welding of titanium alloys: A review. *Mater. Des.* **2018**, *141*, 230–255. [CrossRef]
5. Magudeeswaran, G.; Balasubramanian, V.; Reddy, G.M.; Balasubrarnanian, T.S. Effect of Welding Processes and Consumables on Tensile and Impact Properties of High Strength Quenched and Tempered Steel Joints. *J. Iron Steel Res. Int.* **2008**, *15*, 87–94. [CrossRef]
6. Ramnath, B.V.; Elanchezhian, C.; Rajesh, S.; Prakash, S.J.; Kumaar, B.M.; Rajeshkannan, K. Design and Development of Milling Fixture for Friction Stir Welding. *Mater. Today Proc.* **2018**, *5*, 1832–1838. [CrossRef]
7. Salari, E.; Jahazi, M.; Khodabandeh, A.; Ghasemi-Nanesa, H. Influence of tool geometry and rotational speed on mechanical properties and defect formation in friction stir lap welded 5456 aluminum alloy sheets. *Mater. Des.* **2014**, *58*, 381–386. [CrossRef]
8. Padmanaban, G.; Balasubramanian, V. Selection of FSW tool pin profile, shoulder diameter and material for joining AZ31B magnesium alloy—An experimental approach. *Mater. Des.* **2009**, *30*, 2647–2656. [CrossRef]
9. Huang, O.; Wan, L.; Huang, T.; Lv, Z.; Zhou, L.; Feng, J. The weld formation of self-support friction stir welds for aluminum hollow extrusion. *Int. J. Adv. Manuf. Technol.* **2016**, *87*, 1067–1075. [CrossRef]
10. Węglowski, M.S.; Pietras, A. Friction stir processing-analysis of the process. *Arch. Metall. Mater.* **2011**, *56*, 779–788. [CrossRef]
11. Morisada, Y.; Imaizumi, T.; Fujii, H. Clarification of material flow and defect formation during friction stir welding. *Sci. Technol. Weld. Join.* **2015**, *20*, 130–137. [CrossRef]
12. Kim, Y.G.; Fujii, H.; Tsumura, T.; Komazaki, T.; Nakata, K. Three defect types in friction stir welding of aluminum die casting alloy. *Mater. Sci. Eng. A* **2006**, *415*, 250–254. [CrossRef]
13. Liu, F.C.; Hovanski, Y.; Miles, M.P.; Sorensen, C.D.; Nelson, T.W. A review of friction stir welding of steels: Tool, material flow, microstructure, and properties. *J. Mater. Sci. Technol.* **2018**, *34*, 39–57. [CrossRef]
14. Kumar, R.; Pancholi, V.; Bharti, R.P. Material flow visualization and determination of strain rate during friction stir welding. *J. Mater. Process. Technol.* **2018**, *255*, 470–476. [CrossRef]
15. He, X.; Gu, F.; Ball, A. A review of numerical analysis of friction stir welding. *Prog. Mater. Sci.* **2014**, *65*, 1–66. [CrossRef]
16. Tongne, A.; Desrayaud, C.; Jahazi, M.; Feulvarch, E. On material flow in Friction Stir Welded Al alloys. *J. Mater. Process. Technol.* **2017**, *239*, 284–296. [CrossRef]
17. Yoshikawa, G.; Miyasaka, F.; Hirata, Y.; Katayama, Y.; Fuse, T. Development of numerical simulation model for FSW employing particle method. *Sci. Technol. Weld. Join.* **2012**, *17*, 255–263. [CrossRef]
18. Chen, G.; Li, H.; Wang, G.; Guo, Z.; Zhang, S.; Dai, Q.; Wang, X.; Zhang, G.; Shi, Q. Effects of pin thread on the in-process material flow behavior during friction stir welding: A computational fluid dynamics study. *Int. J. Mach. Tools Manuf.* **2018**, *124*, 12–21. [CrossRef]
19. Zhu, Y.; Chen, G.; Chen, Q.; Zhang, G.; Shi, Q. Simulation of material plastic flow driven by non-uniform friction force during friction stir welding and related defect prediction. *Mater. Des.* **2016**, *108*, 400–410. [CrossRef]
20. Hoyos, E.; López, D.; Alvarez, H. A phenomenologically based material flow model for friction stir welding. *Mater. Des.* **2016**, *111*, 321–330. [CrossRef]

21. Meng, X.; Huang, Y.; Cao, J.; Shen, J.; dos Santos, J.F. Recent progress on control strategies for inherent issues in friction stir welding. *Prog. Mater. Sci.* **2020**, *115*, 100706. [CrossRef]
22. Mishra, R.S.; Ma, Z.Y. Friction stir welding and processing. *Mater. Sci. Eng. R Rep.* **2005**, *50*, 1–78. [CrossRef]
23. Threadgill, P.L.; Leonard, A.J.; Shercliff, H.R.; Withers, P.J. Friction stir welding of aluminium alloys. *Int. Mater. Rev.* **2009**, *54*, 49–93. [CrossRef]
24. Jandaghi, M.R.; Badini, C.; Pavese, M. Dissimilar friction stir welding of AA2198 and AA7475: Effect of solution treatment and aging on the microstructure and mechanical strength. *J. Manuf. Proc.* **2020**, *57*, 712–724. [CrossRef]
25. Dos Santos, J.F.; Staron, P.; Fischer, T.; Robson, J.D.; Kostka, A.; Colegrove, P.; Wang, H.; Hilgert, J.; Bergmann, L.; Hütsch, L.L.; et al. Understanding precipitate evolution during friction stir welding of Al-Zn-Mg-Cu alloy through in-situ measurement coupled with simulation. *Acta Mater.* **2018**, *148*, 163–172. [CrossRef]
26. Asadi, P.; Besharati Givi, M.K.; Akbari, M. Simulation of dynamic recrystallization process during friction stir welding of AZ91 magnesium alloy. *Int. J. Adv. Manuf. Technol.* **2015**, *83*, 301–311. [CrossRef]
27. Yang, C.; Wu, C.S.; Shi, L. Phase-field modelling of dynamic recrystallization process during friction stir welding of aluminium alloys. *Sci. Technol. Weld. Join.* **2020**, *25*, 345–358. [CrossRef]
28. Zenga, X.H.; Xue, P.; Wu, L.H.; Ni, D.R.; Xiao, B.L.; Wang, K.S.; Ma, Z.Y. Microstructural evolution of aluminum alloy during friction stir welding under different tool rotation rates and cooling conditions. *J. Mater. Sci. Technol.* **2019**, *35*, 972–981. [CrossRef]
29. Liu, F.C.; Nelson, T.W. In-Situ grain structure and texture evolution during friction stir welding of austenite stainless steel. *Mater. Des.* **2017**, *117*, 467–478. [CrossRef]
30. Qin, H.; Zhang, H.; Wu, H. The evolution of precipitation and microstructure in friction stir welded 2195-T8 Al–Li alloy. *Mater. Sci. Eng. A* **2015**, *625*, 322–329. [CrossRef]
31. Malopheyev, S.; Vysotskiy, I.; Kulitskiy, V.; Mironov, S.; Kaibyshev, R. Optimization of processing-microstructure-properties relationship in friction-stir welded 6061-T6 aluminum alloy. *Mater. Sci. Eng. A* **2016**, *662*, 136–143. [CrossRef]
32. Gopkalo, O.; Liu, X.; Long, F.; Booth, M.; Gerlich, A.P.; Diak, B.J. Non-isothermal thermal cycle process model for predicting post-weld hardness in friction stir welding of dissimilar age-hardenable aluminum alloys. *Mater. Sci. Eng. A* **2019**, *754*, 205–215. [CrossRef]
33. Fall, A.M.; Monajati, H.; Khodabandeh, A.R.; Fesharaki, M.H.; Champliaud, H.; Jahazi, M. Local mechanical properties, microstructure, and microtexture in friction stir welded Ti-6Al-4V alloy. *Mater. Sci. Eng. A* **2019**, *749*, 166–175. [CrossRef]
34. Huang, Y.; Xie, Y.; Meng, X.; Li, J. Atypical grain coarsening of friction stir welded AA6082-T6: Characterization and modeling. *Mater. Sci. Eng. A* **2019**, *740–741*, 211–217. [CrossRef]
35. Huang, Y.; Xie, Y.; Meng, X.; Li, J.; Zhou, L. Joint formation mechanism of high depth-to-width ratio friction stir welding. *J. Mater. Sci. Technol.* **2019**, *35*, 1261–1269. [CrossRef]
36. Larsson, H.; Karlsson, L.; Stoltz, S.; Bergqvist, E.L. Joining of dissimilar Al-alloys by Friction Stir Welding. In Proceedings of the Second International Conference on Friction Stir Welds, Gothenburg, Sweden, 27–28 June 2000; pp. 1–10.
37. Heurtier, P.; Desrayaud, C.; Montheillet, F. A thermomechanical analysis of the friction stir welding process. *Mater. Sci. Forum* **2002**, *396–402*, 1537–1542. [CrossRef]
38. Krishnan, K. On the formation of onion rings in friction stir welds. *Mater. Sci. Eng. A* **2002**, *327*, 246–251. [CrossRef]
39. Colligan, K. Material flow behaviour during friction welding of aluminum. *Weld. J.* **1999**, *75*, 229–237.
40. Mahoney, M.; Rhodes, C.G.; Flintoff, J.G.; Bingel, W.H.; Spurling, R.A. Properties of friction-stir-welded 7075 T651 aluminum. *Metall. Mater. Trans. A* **1998**, *29*, 1955–1964. [CrossRef]
41. Hamilton, C.; Dymek, S.; Blicharski, M. A model of material flow during friction stir welding. *Mater. Charat.* **2008**, *59*, 1206–1214. [CrossRef]
42. Sutton, M.A.; Yang, B.; Reynolds, A.P.; Taylor, R. Microstructural studies of friction stir welds in 2024-T3 aluminum. *Mater. Sci. Eng. A* **2002**, *323*, 160–166. [CrossRef]
43. Sutton, M.A.; Yang, B.; Reynolds, A.P.; Yan, J. Banded microstructure in 2024-T351 and 2524-T351 aluminum friction stir welds. Part II. Mechanical characterization. *Mater. Sci. Eng. A* **2004**, *364*, 66–74. [CrossRef]

44. Fonda, R.; Reynolds, A.; Feng, C.; Knipling, K.; Rowenhorst, D. Material flow in friction stir welds. *Metall. Mater. Trans. A* **2013**, *44*, 337–344. [CrossRef]
45. Prangnell, P.B.; Heason, C.P. Grain structure formation during friction stir welding observed by the stop action technique. *Acta Mater.* **2005**, *53*, 3179–3192. [CrossRef]
46. Schneider, J.A.; Nunes, A.C. Characterization of plastic flow and resulting microtextures in a friction stir weld. *Metall. Mater. Trans. B* **2004**, *35*, 777–783. [CrossRef]
47. Elangovan, K.; Balasubramanian, V.; Valliappan, M. Effect of Tool Pin Profile and Tool Rotational Speed on Mechanical Properties of Friction Stir Welded AA6061 Aluminium Alloy. *Mater. Manuf. Proc.* **2008**, *23*, 251–260. [CrossRef]
48. Sharma, C.; Dwivedi, D.K.; Kumar, P. Effect of welding parameters on microstructure and mechanical properties of friction stir welded joints of AA7039 aluminum alloy. *Mater. Des.* **2012**, *36*, 379–390. [CrossRef]
49. Guo, H.C.; Chen, C.N.; Sun, G.; Bi, Z.; Sun, J. Friction stir welding of dissimilar materials between AA6061 and AA7075 Al alloys effects of process parameters. *Mater. Des.* **2014**, *56*, 185–192. [CrossRef]
50. Guduru, R.K.; Darling, K.A.; Kishore, R.; Scattergood, R.O.; Koch, C.C.; Murty, K.L. Evaluation of mechanical properties using shear–punch testing. *Mater. Sci. Eng. A* **2005**, *395*, 307–314. [CrossRef]
51. Lucas, G. The development of small specimen mechanical test techniques. *J. Nucl. Mater.* **1983**, *117*, 327–339. [CrossRef]
52. Zoghlami, M. Influence des Paramètres du Procédé FSW sur les Caractéristiques des Bandes Alternées (Onion Rings) dans les Alliages D'aluminium. Master's Thesis, École de Technologie Supérieure, Montreal, QC, Canada, 2017.
53. Genevois, C.; Deschamps, A.; Denquin, A.; Cottignies, B.D. Quantitative investigation of precipitation and mechanical behaviour for AA2024 friction stir welds. *Acta Mater.* **2005**, *53*, 2447–2458. [CrossRef]
54. Svensson, L.E.; Karlsson, L.; Larsson, H.; Karlsson, B.; Fazzini, M.; Karlsson, J. Microstructure and mechanical properties of friction stir welded aluminium alloys with special reference to AA 5083 and AA 6082. *Sci. Technol. Weld. Join.* **2000**, *5*, 285–296. [CrossRef]
55. Liu, C. Microstructure Evolution during Homogenization and Its Effect on the High Temperature Deformation Behaviour in AA6082 Based Alloys. Ph.D. Thesis, University of British Columbia, Vancouver, BC, Canada, 2017.
56. De Filippis, L.; Serio, L.; Palumbo, D.; De Finis, R.; Galietti, U. Optimization and characterization of the Friction Stir Welded Sheets of AA 5754-H111: Monitoring of the quality of joints with thermographic techniques. *Materials* **2017**, *10*, 1165. [CrossRef]
57. Tang, W.; Guo, X.; McClure, J.C.; Murr, L.E.; Nunes, A. Heat Input and Temperature Distribution in Friction Stir Welding. *J. Mater. Proc. Manuf. Sci.* **1998**, *7*, 163–172. [CrossRef]
58. Liu, F.C.; Ma, Z.Y. Influence of tool dimension and welding parameters on microstructure and mechanical properties of friction-stir-welded 6061-T651 aluminum alloy. *Metall. Mater. Trans. A* **2008**, *39*, 2378–2388. [CrossRef]
59. Woo, W.; Choo, H.; Brown, D.W.; Feng, Z. Influence of the Tool Pin and Shoulder on Microstructure and Natural Aging Kinetics in a Friction-Stir-Processed 6061–T6 Aluminum Alloy. *Metall. Mater. Trans. A* **2007**, *38*, 69–76. [CrossRef]
60. Sato, Y.S.; Kokawa, H.; Ikeda, K.; Enomoto, M.; Hashimoto, T.; Jogan, S. Microtexture in the friction-stir weld of an aluminum alloy. *Metall. Mater. Trans. A* **2001**, *32*, 941–948. [CrossRef]
61. Frigaard, Ø.; Grong, Ø.; Midling, O.T. A process model for friction stir welding of age hardening aluminum alloys. *Metall. Mater. Trans. A* **2001**, *32*, 1189–1200. [CrossRef]
62. Nakamura, T.; Obikawa, T.; Nishizaki, I.; Enomoto, M.; Fang, Z. Friction Stir Welding of Non-Heat-Treatable High-Strength Alloy 5083-O. *Metals* **2018**, *8*, 208. [CrossRef]
63. Hornbuckle, B.C.; Murdoch, H.A.; Roberts, A.J.; Kecskes, L.J.; Tschopp, M.A.; Doherty, K.J.; Yu, J.H.; Darling, K.A. Property mapping of friction stir welded Al-2139 T8 plate using site specific shear punch testing. *Mater. Sci. Eng. A* **2017**, *682*, 192–201. [CrossRef]